An Immersed Boundary Based Dynamic Contact Angle Framework for Handling Complex Surfaces of Mixed Wettabilities

(article starts on next page)

An immersed boundary based dynamic contact angle framework for handling complex surfaces of mixed wettabilities

Johan Göhl[a], Andreas Mark[*, a], Srdjan Sasic[b], Fredrik Edelvik[a]

[a] *Fraunhofer-Chalmers Centre, Chalmers Science Park, Gothenburg SE-412 88, Sweden*
[b] *Division of Fluid Dynamics, Chalmers University of Technology, Gothenburg SE-412 96, Sweden*

ABSTRACT

We propose a comprehensive immersed boundary-based dynamic contact angle framework capable of handling arbitrary surfaces of mixed wettabilities in three dimensions. We study a number of dynamic contact angle models and implement them as a boundary condition for the Continuum Surface Force method. Special care is taken to capture the contact angle hysteresis by using separate models for the advancing and receding contact lines. The framework is able to account for surfaces of varying wettability by making the contact angle dependent on the local boundary condition.

We validate our framework using cases where glycerol droplets impact solid surfaces at low Weber numbers. We show how a truly dynamic contact angle model is needed for advancing contact lines and how a separate dynamic model is needed for receding contact lines. To test our framework for industrially relevant problems on a more complex surface, we simulate droplet impact on a printed circuit board. We show how the local surface properties control the final droplet deposition and that the framework is capable of handling adjacent surfaces of considerably different wettabilities.

© 2018.

1. Introduction

The role of the dynamic contact angle in spreading fluids is very important when surface tension forces are significant compared to inertia and viscous forces. This is the case in several different industrial applications, ranging from coating processes (Yan et al., 2017) to the relatively new areas of superhydrophobic surfaces (Lalia et al., 2017) and 3D-bioprinting (Göhl et al., 2018). One in particular important area of the wetting phenomena is the dynamics of droplets as the latter impact and spread on solid surfaces (Zhao et al., 2017), which is crucial for industrial applications such as spray coating (Pasandideh-Fard et al., 2002; Andrade et al., 2013; Sharifahmadian et al., 2013), spray cooling (Chandra et al., 1996; Bostanci et al., 2009), aerodynamics (Mangini et al., 2015) and ink-jet printing (Soltman et al., 2013). The spreading of fluids on solid surfaces is governed by the dynamics of the three phase contact line, which is the line where two immiscible fluids and the solid surface meet. The contact angle, θ, is measured through the heavier fluid at the three phase contact line and influences how the fluid will spread on the solid surface and consequently the equilibrium state of the fluid. With a moving three phase contact line, as in spreading of droplets, the contact angle, θ_D, is dynamic and deviates significantly from the equilibrium value, θ_E (Johnson et al., 1977). The importance of surface tension, and in particular dynamic contact angles, in

these cases is quantified by a low impact Weber number and/or a low capillary number. At these conditions, the utilisation of an accurate dynamic contact angle model is crucial to capture the dynamics of spreading and receding contact lines.

The framework for dynamic contact angles is implemented in the in-house state-of-the-art multiphase flow solver IBOFLOW (Mark and van Wachem, 2008; Mark et al., 2011), developed by the Fraunhofer–Chalmers research centre and used to successfully simulate a number of different industrial applications (Svenning et al., 2012; Johnson et al., 2016; Mark et al., 2013; 2014). IBOFLOW uses the volume-of-fluid (VOF) method (Hirt and Nichols, 1981) to model the two phase flow, where the CICSAM (Ubbink and Issa, 1999) convective scheme is used to keep the fluid-fluid interface sharp. This macroscopic approach for modeling of contact angles does not resolve the molecular scale interactions between the fluids and the solid at the three phase contact line, but, by using a balance of macroscopic forces, the approach is found to reproduce the results of the microscale interactions quite well (Rosengarten et al., 2006).

The use of VOF within CFD simulations to accurately capture the dynamics of wetting phenomena has been investigated in several studies. Probably the first study to use 3D numerical simulations of impact and spreading of droplets on solid surfaces was the one by Bussmann et al. (2000). In that study the dynamics of the contact angle were modeled by a linear relation to the contact line velocity, which was evaluated one half cell above the solid surface. However, a linear relation between the dynamic contact angles and the contact line velocity is not ideal, and does not translate easily between different liquids. Therefore we have chosen in this work to use four different dynamic

contact angle models based on the contact line velocity and the physical properties of the liquid. Another study of droplet impact using VOF, which used dynamic contact angle models dependent on the contact line velocity, is the one of Šikalo et al. (2005b). The numerical simulations in that study were 3D and axisymmetric, enabling the contact line velocity to equal the time derivative of the wetted radius. The method produced accurate results of droplet impact, but with the drawback of being limited to axisymmetric wetting applications. A slightly more general approach was taken in Malgarinos et al. (2014), where the contact line velocity is based on the actual cell velocity at the contact line, to successfully simulate droplet impact. The dynamic contact angles were derived implicitly from the interface shape, and not employed as a boundary condition, making the method limited to axisymmetric simulations. In Roisman et al. (2008), a method was developed that uses the instantaneous velocity at the contact line as an input to the dynamic contact angle models. The method is 2D and axisymmetric, but with the potential of being extended to a more general 3D case.

A crucial factor for a method to work in non-axisymmetric applications is the calculation of the contact line velocity. We use the cell velocity at the contact line in this work, which is, to some extent, affected by the no-slip condition at the wetted surface. Both Renardy et al. (2001) and Afkhami et al. (2009) investigated the mesh-dependent implicit slip along no-slip boundaries, noting that the contact line motion is hindered if the grid size becomes too small, but that a solution to the wetting of the surface is obtained on coarser grids. To achieve a fine resolution of the grid, without hindering the motion of the contact line, there are several techniques available, such as the diffuse interface approach (Liu and Ding, 2015) or slip boundary conditions (Dussan V., 1976). We use a Navier-slip boundary condition, as previously done by Renardy et al. (2001) and Afkhami et al. (2009), to address this issue. In Šikalo et al. (2005b), Malgarinos et al. (2014) and Roisman et al. (2008), no difference was made between an advancing and a receding contact line, and the same dynamic contact angle model was used for both cases. As we will explain in the next section, this causes a non-physical behaviour of the contact line, as the receding contact angle should decrease with increasing the contact line velocity. Therefore, we use two different dynamic contact angle models in our work, one advancing and one receding, in order to account for contact angle hysteresis.

In this work we propose an immersed boundary based framework for dynamic contact angles with the capability to handle arbitrary surfaces of different wettabilities. For the employment of contact angles we have chosen to follow Brackbill et al. (1992) and Ubbink (1997), where the dynamic contact angle model is inserted as a boundary condition for the Continuum Surface Force method. To enable non-axisymmetric simulations, we take the contact line velocity from the center of the cells at the contact line. We conduct grid-size and time-step convergence studies on glycerol droplets impacting a surface to validate the implemented framework. To further validate and evaluate the framework, we use four different dynamic contact angle models for the advancing contact lines and compare the results to experimental data from Šikalo et al. (2005a) and German and Bertola (2009), both involving glycerol droplets impacting a solid surface. We also show the importance of a separate dynamic contact angle model for receding contact lines to capture contact angle hysteresis. To demonstrate the ability of the framework to handle complex surface geometries and adjacent surfaces of mixed wettabilities, we have formulated a showcase with a droplet impacting a printed circuit board.

2. Wettability

For all combinations of two immiscible fluids on solid surfaces there is a specific equilibrium contact angle. The angle is related to all the different surface tension forces present at the three phase contact line through Young's equation (Young, 1805),

$$\sigma_{l-g} \cos\left(\theta_E\right) = \sigma_{s-g} - \sigma_{l-s}, \tag{1}$$

where σ_{l-g} is the surface tension between liquid and gas, σ_{s-g} is between solid and gas and σ_{l-s} is between solid and liquid. The wettability is high if the equilibrium contact angle is small, $\theta_E \ll 90°$. Large contact angles, $\theta_E \gg 90°$, yield low wettability. The equilibrium contact angle is a static contact angle that is in between the advancing contact angle, θ_A, and the receding contact angle, θ_R. The advancing contact angle is the largest static contact angle just before the three phase contact line starts wetting the surface, while the receding angle is the smallest static contact angle just before the three phase contact line starts receding (Johnson et al., 1977). The range of static angles found in between the advancing and receding contact angles is called the contact angle hysteresis. A good example of contact angle hysteresis is a rain drop resting on a vertical window, as seen in Fig. 1. The contact angle hysteresis acts to keep the droplet in place, while gravity pulls it down and the result is an asymmetric droplet shape with a small contact angle at the top, θ_R, and a large contact angle at the bottom, θ_A. If an additional force is added to move the droplet downwards, the contact angle will exceed θ_A and the droplet starts sliding. The contact line, as well as the contact angle, is now dynamic, and the contact angles will deviate from the static values of θ_A and θ_R. The advancing contact angle of the droplet will increase with increasing the contact line velocity, V_{cl}, while the receding contact angle will decrease with increasing the contact line velocity.
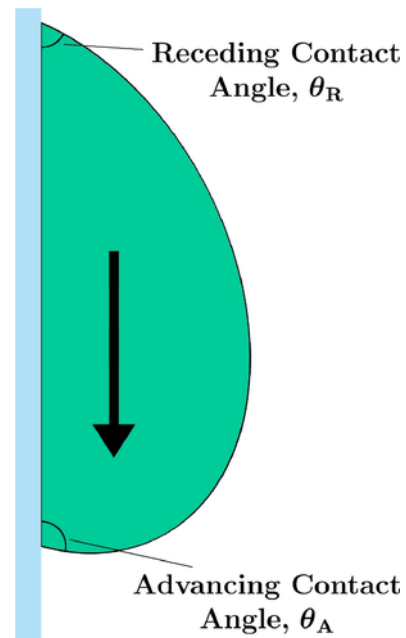

Fig. 1. A rain drop resting on a window. Contact angle hysteresis acts to keep the droplet in place while gravity is pulling it down.

2.1. Dynamic contact angle models

A dynamic contact angle model is employed as a boundary condition at the moving three phase contact line to better predict the surface tension governed flows. This is trivial for a static contact angle, which is a material property, but the dynamic contact angle depends on a long list of variables (Šikalo et al., 2005b; Kistler, 1993),

$$\theta_D = f\left(\theta_E, \text{Ca}, \text{We}, \mu_l \ldots\right), \tag{2}$$

where μ_l is the dynamic liquid viscosity. Ca is the Capillary number defined as

$$\text{Ca} = \frac{V_{cl}\mu_l}{\sigma_{l-g}} = \frac{\text{Viscous forces}}{\text{Surface tension}}, \tag{3}$$

where V_{cl} is the contact line velocity. We is the Weber number defined as

$$\text{We} = \frac{u^2 \rho_l D}{\sigma_{l-g}} = \frac{\text{Liquid"s inertia}}{\text{Surface tension}}, \tag{4}$$

where u is the impact velocity, ρ_l is the liquid density and D is the droplet diameter.

The long list of factors influencing the dynamic contact angle makes modeling difficult, but there are some experimental observations that can be utilised. The most important one is that the dynamic contact angle increases with increasing the contact line velocity for spreading liquids. The second important observation is that the dynamic contact angle increases more rapidly for more viscous liquids (Kistler, 1993). From these observations several empirical dynamic contact angle models have been proposed, where a commonly used model is the Hoffman-Voinov-Tanner law:

$$\theta_D^3 = c_T \text{Ca}, \tag{5}$$

which is valid for Ca<1, and where c_T is a constant assumed to be around 72 rad[3] (Hoffman, 1975). Four different dynamic contact angle models are compared in this paper, one quasi-dynamic and three truly dynamic models. These dynamic contact angle models are only applied on advancing contact lines, in which the contact angle increases with increasing contact line velocity. As for the receding contact line, several other works, for example Šikalo et al. (2005b), Malgarinos et al. (2014), Roisman et al. (2008) and Ashish Saha and Mitra (2009), use the same dynamic model as for the advancing contact line. This causes the dynamic contact angle to increase with the increasing receding velocity, which is the opposite of how it is supposed to work. Therefore we use a separate dynamic model for the receding contact lines, in which the dynamic contact angle decreases with increasing the contact line velocity. This captures the dynamics of the contact angle, and makes it possible to capture the contact angle hysteresis, in which the contact angles acts to keep the contact line in place.

2.1.1. Quasi-dynamic contact angle model

The quasi-dynamic model is the most basic dynamic contact angle model and is based on if the three phase contact line is advancing or re-

ceding. Since there is only a dependence on the contact line direction, two basic equations govern this model

$$\begin{aligned} \theta_D &= \theta_A, \quad \text{if} \quad \vec{V}_{cl} \text{ is advancing,} \\ \theta_D &= \theta_R, \quad \text{if} \quad \vec{V}_{cl} \text{ is receding,} \end{aligned} \tag{6}$$

where the contact angle hysteresis is accounted for, but the dynamics of a spreading contact line are not. If no experimental data of contact angle hysteresis are available, the model is reduced to a static model,

$$\theta_D = \theta_E. \tag{7}$$

2.1.2. Kistler's dynamic contact angle model

The empirical dynamic contact angle model developed by Kistler (1993) is based on Hoffman's empirical function (Hoffman, 1975). In this correlation the dynamic contact angle is dependent on the static contact angle and the contact line velocity through the Ca number. The model is valid for advancing contact lines and is given in the form

$$\theta_D = f_H\left(\text{Ca} + f_H^{-1}\left(\theta_E\right)\right), \tag{8}$$

where $f_H(x)$ is Hoffman's empirical function and $f_H^{-1}(x)$ is its inverse. Hoffman's empirical function is defined as

$$\begin{aligned} &f_H(x) \\ &= \cos^{-1}\left(1 - 2\tanh\left(5.16\left(\frac{x}{1 + 1.31x^{0.99}}\right)^{0.706}\right)\right), \end{aligned} \tag{9}$$

and the inverse of Hoffman's empirical function is closely approximated by the Hoffman-Voinov-Tanner law, Eq. (5), and has the form

$$f_H^{-1}\left(\theta_E\right) = \frac{\theta_E^3}{c_T}. \tag{10}$$

If experimental data of the contact angle hysteresis are available, the static contact angle, θ_E, in equations (8) and (10) is replaced by θ_A if the contact line is advancing. The final form of the model used for the advancing contact lines is

$$\theta_D = f_H\left(\text{Ca} + f_H^{-1}\left(\theta_A\right)\right). \tag{11}$$

2.1.3. Shikhmurzaev's model

The second empirical model used in this work is a reduced version of Shikhmurzaev's *Full interface formation model* (Shikhmurzaev, 2008). This model is also dependent on the contact line velocity, through the Ca number, and the equilibrium contact angle. But, it is also dependent on three phenomenological constants fitted to experiments. The model utilises a theory that the solid-liquid and the liquid-gas interfaces have specific thermodynamic properties, which means that they behave like true phases, and the contact line motion is a result of mass exchange between these two phases (Popescu et al., 2008).

To derive the model, the well known Young's equation, (1), is converted to a dynamic Young's equation by replacing the static contact

angle with the dynamic contact angle,

$$\sigma_{l-g} \cos\left(\theta_D\right) = \sigma_{s-g} - \sigma_{l-s}. \tag{12}$$

The above equation is then used as a boundary condition in the system of governing equations, Eq. (22), for the case when the displaced gas is inviscid. In this case, there are asymptotic limits where an analytical solution can be found (Shikhmurzaev, 1994). The limit used to derive Shikhmurzaev's model is a steady motion at low Ca and Re numbers, and that the flow at the three phase contact line is unaffected by flows at other closely located boundaries. This leads to the algebraic equation

$$\cos\left(\theta_D\right) = \cos\left(\theta_A\right) - \frac{2u\left(a_1 + a_2 u_0\right)}{(1 - a_2)\left(\left(a_1 + u^2\right)^{1/2} + u\right)}, \tag{13}$$

which is also known as Shikhmurzaev's model, valid at small Ca numbers and for advancing contact lines. a_1 is a constraint for the equilibrium state of the system, following from Eq. (1), u_0 is the radial velocity at the liquid-gas interface moving with the three phase contact line, u is the dimensionless three phase contact line velocity, and a_2 is the dimensionless surface density. The parameter a_1 is calculated as

$$a_1 = 1 + (1 - a_2)\left(\cos\left(\theta_A\right) - a_4\right), \tag{14}$$

where a_4 is the dimensionless surface tension in the gas-solid interface. The radial velocity u_0 is estimated as

$$u_0 = \frac{\sin\left(\theta_D\right) - \theta_D \cos\left(\theta_D\right)}{\sin\left(\theta_D\right)\cos\left(\theta_D\right) - \theta_D}, \tag{15}$$

and the dimensionless three phase contact line velocity, u is defined as

$$u = a_3 \mathrm{Ca} = a_3 \frac{V_{cl}\mu_l}{\sigma_{l-g}}, \tag{16}$$

where a_3 is the scale factor. The phenomenological constants used in the model are fitted parameters from experiments. For the case of glycerol there are experiments conducted in Blake and Shikhmurzaev (2002) with the resulting phenomenological constants

$$a_2 = 0.63, \quad a_3 = 4.3 \quad a_4 = -0.08.$$

For an advancing contact line, the model becomes

$$\theta_D = \cos^{-1}\left(\cos\left(\theta_A\right) - \frac{2u\left(a_1 + a_2 u_0\right)}{(1 - a_2)\left(\left(a_1 + u^2\right)^{1/2} + u\right)}\right). \tag{17}$$

2.1.4. Cox's model

The third truly dynamic contact angle model used is based on the asymptotic theory developed by Cox (1986), Hocking and Rivers (1982), Ngan and Dussan V. (1982) and Dussan et al. (1991), and is valid for both advancing and receding contact lines. It has the form

$$\theta_D = g^{-1}\left(g\left(\theta_{app}\right) + \mathrm{Ca}\log\left(\frac{L}{\lambda}\right)\right), \tag{18}$$

for two fluids of arbitrary viscosity, where θ_{app} is the apparent contact angle in the macroscopic region, L is the apparent length and λ is the physical slip length. The function $g(\theta)$ simplifies to

$$g(\theta) = \int_0^\theta \frac{x - \sin x \cos x}{2\sin x}dx, \tag{19}$$

when the surrounding fluid is of much smaller viscosity, as with the case of air and glycerol/water-mixtures. The function g and its inverse g^{-1} can be approximated with fitting polynomials as proposed by Mathieu (2003),

$$\begin{aligned} g(x) &\approx x^3/9 - 0.00183985x^{4.5} + 1.845823 \times 10^{-6} \times x^{12.258487}, \\ g^{-1}(x) &\approx 9x^{1/3} + 0.0727387x - 0.0515388x^2 + 0.00341336x^3, \end{aligned} \tag{20}$$

and previously used by Dupont and Legendre (2010), Maglio and Legendre (2014) and Legendre and Maglio (2015).

In Eq. (18), the apparent length, L, is imposed as half the minimum grid size (Legendre and Maglio, 2015), which is equal to the actual slip length, and the physical slip length, λ, is set to 10^{-9} m (Sui and Spelt, 2013). The apparent contact angle, θ_{app}, can either be obtained from empirical correlations where θ_{app} is dependent on Ca and θ_E, such as used in Afkhami et al. (2009) and Sui and Spelt (2013), or by using the known θ_E as θ_{app} as in Legendre and Maglio (2015). In our work we have chosen the latter, and impose θ_A or θ_R as θ_{app} depending on if the contact line is advancing or receding. If the contact line is receding, the Ca number will be calculated with a negative V_{cl} which will ensure a decreasing θ_D with increasing contact line velocity during the receding phase.

As noted in Sui et al. (2014), this model is not well suited for simulations of highly curved moving contact lines in three dimensions, since the asymptotic results of Cox (1986) and Cox (1998), on which the model is built, are not applicable. In practice, this should not be of any concern for axisymmetric droplet impact on a flat surface.

2.1.5. Dynamic receding contact angle model

To account for contact angle hysteresis and make the dynamic contact angle decrease during the receding phase, a dynamic receding contact angle model is needed. The model chosen is based on the correlation of Tanner (1979) and was first presented in Nichita et al. (2010). The model is dependent on the contact line velocity through the Ca number and reads

$$\theta_D = \left(\theta_R - 72\mathrm{Ca}\right)^{1/3}. \tag{21}$$

This model is used as the receding model for both Kistler's and Shikhmurzaev's models.

3. Governing equations

The Navier–Stokes equations model the motion of incompressible two-phase flow:

$$\nabla\cdot\vec{v} = 0,$$
$$\rho\left(\frac{\partial\vec{v}}{\partial t} + \nabla\vec{v}\cdot\vec{v}\right) = -\nabla P + \nabla\cdot\mu\left(\nabla\vec{v} + \left(\nabla\vec{v}\right)^T\right) + \rho\vec{g} + \vec{f}_\sigma, \quad (22)$$

where v_i is the velocity, P is the pressure, g_i is the volume (gravitational) force and f_σ is the additional surface tension force. The VOF method is used to track the interface between immiscible fluids. It models two-phase flows by using volume fractions, α, to identify each phase separately. The density and viscosity in grid cells are calculated according to

$$\rho = \alpha\rho_l + (1-\alpha)\rho_g,$$
$$\mu = \alpha\mu_l + (1-\alpha)\mu_g. \quad (23)$$

The distribution of the liquid volume fraction, and consequently tracking of the liquid-gas interface, is solved by a separate transport equation for the volume fraction advection,

$$\frac{\partial\alpha}{\partial t} + \nabla\cdot\left(\alpha\vec{v}\right) = 0. \quad (24)$$

The Navier-Stokes equations, Eq. (22), together with the volume fraction advection, (24), are solved using IBOFLOW®, a finite volume based incompressible flow solver. The equations are discretized on a dynamic Cartesian octree grid that can be dynamically refined to get a higher resolution of the fluid-fluid interface or close to immersed objects. The grid is automatically built and connected to the triangulated objects, hence no time consuming prepossessing of the grid is necessary, which makes the solver very practical to use. IBOFLOW uses a sequential solution method in which Eq. (24) is solved first, at the beginning of each time step. The volume fraction is then used to update the density and viscosity in each grid cell according to Eq. (23) before solving the Navier-Stokes equations. A segregated solution technique, the SIMPLEC method (Van Doormaal and Raithby, 1984), of the Navier-Stokes equations is employed to couple the velocity and pressure fields. All variables are stored in a co-located grid arrangement and the pressure-weighted flux interpolation by Rhie and Chow (1983) is used to prevent pressure oscillations. The Compressive Interface Capturing Scheme for Arbitrary Meshes (CICSAM) (Ubbink and Issa, 1999) is used for the discretisation of Eq. (24). All triangulated objects are handled with the mirroring immersed boundary method (Mark and van Wachem, 2008) and the local intersections of the triangulation are stored to support the surface tension force calculations.

3.1. Surface tension force model

The surface tension force term in Eq. (22) is modeled using the Continuum Surface Force method by Brackbill et al. (1992). The surface tension force across the liquid-gas interface is approximated by a body force, which acts throughout a small but finite fluid region surrounding the interface. The equation reads

$$\vec{f}_\sigma = \sigma\kappa\nabla\alpha, \quad (25)$$

where κ is the curvature of the liquid-gas interface. The curvature is approximated as the divergence of the interface normal,

$$\kappa = \nabla\cdot\hat{n}, \quad (26)$$

where $\hat{n}$ is the interface normal, which is in turn approximated by the normalised volume fraction gradient

$$\hat{n} = \frac{\nabla\alpha}{|\nabla\alpha|}. \quad (27)$$

In order to calculate the divergence of the interface normal of a cell, the volume fraction gradient needs to be calculated for all faces of the cell. For fluid cells not in contact with any immersed boundary object or fluid boundary, the gradient is calculated by a linear interpolation between neighbouring cells. But for cells at the three phase contact line, the interface normal is used for applying contact angles, and the methodology is explained in next section.

4. Implementation

4.1. Static contact angle model

The static contact angle is implemented as a boundary condition for the continuum surface force method by altering the interface curvature at cell faces neighbouring an exterior or an immersed boundary wall or surface. The interface curvature is calculated by (26), but in cells adjacent to a surface this expression is altered in order to insert a contact angle by rotating the interface curvature. This is done according to Brackbill et al. (1992) and Ubbink (1997), where the interface normal in surface boundary cell faces is calculated as

$$\hat{n}_f = \hat{n}_s\cos\left(\theta_E\right) + \hat{n}_t\cos\left(\theta_E\right), \quad (28)$$

where $\hat{n}_s$ is the surface normal and $\hat{n}_t$ is the tangential surface normal pointing along the surface, into the liquid. If a cell face is neighbouring a boundary wall of the computational domain, the surface normal is simply extracted from the boundary condition. If the cell face instead is neighbouring an immersed boundary object, the normals from triangles intersecting the cell are extracted from the triangulation and weighted by the intersecting triangle area. The extracted normals are summarised and normalised to yield the surface normal required. The direction of the tangential surface normal is given by

$$\hat{n}_t = \hat{n}_s\times\frac{\nabla\alpha}{|\nabla\alpha|}\times\hat{n}_s. \quad (29)$$

A number of selection rules need to be established in order to filter out the cells in which the static contact angle is to be inserted. The cells adjacent to a surface and in the immediate vicinity of the liquid-gas interface should be selected. This definition is dependent on the magnitude of the volume fraction gradient, $\nabla\alpha$, in the direction of the contact line. The component of $\nabla\alpha$ going out from the surface is therefore of no interest, and the volume fraction gradient is projected down onto the plane of the surface as

$$\nabla\alpha_{\parallel\hat{n}_s} = \hat{n}_s\times\nabla\alpha\times\hat{n}_s = \nabla\alpha_s. \quad (30)$$

The numerical selection is then made based on the maximum value of $|\nabla \alpha_s|$ alongside the surface, so for surface boundary cells which fulfil

$$|\nabla \alpha_s| \geq 0.5 \, |\nabla \alpha_s|_{max} \qquad (31)$$

the static contact angle is inserted, resulting in approximately 1 to 4 cells with contact angles across the interface depending on the interface resolution.

4.2. Dynamic contact angle model

The dynamic contact angle model utilises all the components of the static model, but the static contact angle in Eq. (28) is replaced by a dynamic contact angle, θ_D, calculated from one of the models presented in Section 2.1. In order for the dynamic models to work, there must be a way to estimate the direction and magnitude of the contact line velocity. For axisymmetric simulations there are accurate and simple ways of estimating that velocity, such as the time derivative of the wetted radius. Such a procedure is not viable for non-axisymmetric cases, and thus a more general method is required. The approach chosen here is based on actual cell velocities, $\vec{u}_{cell}$, of which the velocity component parallel to the surface is used to estimate the contact line velocity. This is the same approach as used in Malgarinos et al. (2014) but extended to work in three dimensions at immersed boundaries as well,

$$\vec{V}_{cl} = \vec{u}_{cell} \left\| \hat{n}_s = \hat{n}_s \times \vec{u}_{cell} \times \hat{n}_s. \right. \qquad (32)$$

This method is straightforwardly implemented and works well in both two-dimensional and three dimensional cases, but with the drawback of not being as accurate as the axisymmetric alternative. The contact line velocities are taken from the liquid side of the interface, $\alpha \geq 0.5$, and then extrapolated to the cells dominated by gas, $\alpha < 0.5$. This is a good approximation, since the contact line velocity is better approximated by the heavier fluid (Roisman et al., 2008). Another known issue associated with dynamic contact angle models, and more specifically with the estimation of the contact line velocity, is the non-integrable stress singularity (Legendre and Maglio, 2015; Holmgren, 2015), which arises when a moving contact line spreads on a no-slip boundary. The stress generated by a moving contact line can be estimated as

$$\tau_{xy} = \mu_l \frac{V_{cl}}{\Delta x}, \qquad (33)$$

where Δx is the grid spacing at the boundary. For fine grids the stress is diverging, hindering the motion of the contact line. In our work, a Navier-slip boundary condition is chosen to relax the no-slip boundary. The implementation is according to Ferrás et al. (2013) and the slip length, which defines the extent of the relaxation, is set equal to half the minimum grid size, as proposed by Afkhami et al. (2009) and Renardy et al. (2001).

The direction of the contact line velocity is also needed in order to establish if the interface is advancing (spreading) or receding (recoiling). This is achieved by calculating a dot product between the volume fraction gradient and the contact line velocity.

$$\begin{array}{lll} \text{Advancing } \vec{V}_{cl}, & \text{if} & \vec{V}_{cl} \cdot \nabla \alpha \leq 0 \\ \text{Receding } \vec{V}_{cl}, & \text{if} & \vec{V}_{cl} \cdot \nabla \alpha > 0 \end{array} \qquad (34)$$

5. Numerical results

The implementation of dynamic contact angle models into IBOFLOW is verified thoroughly by both grid size and time step convergence studies. The simulations are of glycerol/water droplets impacting a solid surface at low impact Weber numbers, a case with experimental data from Šikalo et al. (2005a) and German and Bertola (2009). The same experimental data are also used for comparison between the different dynamic contact angle models.

The simulations are performed in three dimensions and the computational domain consists of $20 \times 20 \times 10$ identical hexahedral cells, where each side of the cell is $0.4 \, \text{mm}$. Two different boundary conditions are used in the simulations. The top boundary in the z-direction is a pressure outlet of 101 325 Pa, and all other boundaries are set to no-slip walls. The initial droplet diameter, D_0, is set to 2.45 mm in accordance with Šikalo et al. (2005a). The initial droplet velocity in the negative z-direction, U_0, is varied between 0.2 m/s and 2 m/s based on the desired impact Weber number. The droplet's initial position is centered just above the solid surface. The rest of the computational domain is filled with air, with the physical properties $\rho_g = 1.2 \, \text{kg/m}^3$, $\mu_g = 0.001 \, \text{Pas}$ and $\sigma_g = 0.073 \, \text{N/m}$. A gravitational force of 9.81 m/s^2 is added in the negative z-direction.

5.1. Validation of framework

The grid and time convergence studies are conducted to test the performance of the implemented framework. Only Shikhmurzaev's dynamic contact angle model is used in the convergence studies since all four models are based on the same framework. A droplet of 85 vol-% glycerol and 15 vol-% water, is simulated as it impacts a solid surface. The simulations are terminated when the first spreading phase is over. Physical data of the glycerol droplet are found in Šikalo et al. (2005a) and presented in Table 1. The parameter calculated during the simulations is the spread factor, β, which is the diameter of the wetted spot, d, divided by the initial diameter of the droplet D_0,

$$\beta = \frac{d}{D_0}. \qquad (35)$$

5.1.1. Grid convergence

The evolution of the spread factor for a glycerol droplet impacting a solid surface at We = 51 is compared for four different levels of minimum grid size, Δx_{min}. Adaptive local grid refinements of fluid-fluid interface cells are used in order to reduce the total number of cells, splitting cells on both sides of the interface into 8 new cells. The different levels of refinements used and the resulting minimum grid size, Δx_{min}, are presented in Table 2. An adaptive time step is used, with a fixed fluid Courant number of 0.125. The average time step, $\overline{\Delta t}$, for each level of grid size is also presented in Table 2. To achieve a high resolution of the moving contact line, but still avoid the stress divergence at the moving contact line, a Navier-slip boundary condition is used to relax the no-slip boundary condition on the surface.

Table 1
Physical properties of 85 vol-% glycerol droplet used in convergence studies.

D_0	ρ	μ	σ	θ_A	θ_R
(mm)	(kg/m^3)	(Pa s)	(N/m)	(°)	(°)
2.45	1220	0.116	0.063	17	13

Table 2
Numerical parameters used in grid convergence study.

Refinements	Δx_{min}	CFL	$\overline{\Delta t}$
1	0.2 mm	0.125	1.5×10^{-2} ms
2	0.1 mm	0.125	6.5×10^{-3} ms
3	0.05 mm	0.125	2.2×10^{-3} ms
4	0.025 mm	0.125	8.2×10^{-4} ms

As seen in Fig. 2, the implemented framework shows a grid convergence. For the coarsest grid, the droplet spreads considerably further than for the other grids. For finer Δx_{min} the results of β starts to converge, and the implemented framework converges at the two finest grids tested. However, a minor grid dependence is still seen during the initial spreading. This initial divergence has previously been noted by Legendre and Maglio (2015), who concluded that it is a result of the finite volume integration of the Continuum Surface Force method.

In Fig. 3 we investigate the grid dependence of the dynamic contact angle and the contact line velocity. As expected, a grid dependence can be seen for both the contact line velocity and the dynamic   contact   an-
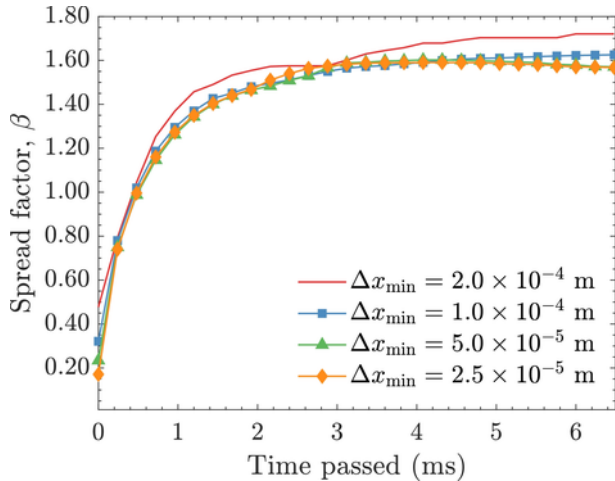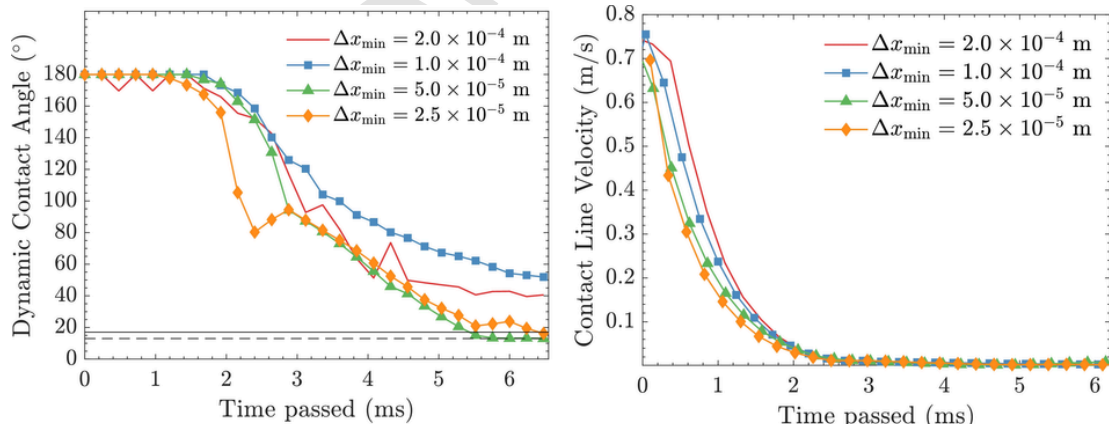

Fig. 2. Results of the spread factor evolution for the grid convergence study. Four different levels of minimum grid size are investigated.

gle. The differences can in part be explained by the increasingly finer resolution across the contact line at which we gather the data. On the two finest Δx_{min}, an end to the first spreading phase is observed, with values of the dynamic contact angle close to or below the equilibrium contact angles. Regarding the contact line velocity the trend is showing a decreasing contact line velocity for finer grids, which is converging for the latter part of the spreading phase. During the initial spreading, the contact line velocity shows grid dependence. This is probably also in part due to the finite volume integration of the Continuum Surface Force method, as noted previously.

5.1.2. Time convergence

As with the grid convergence, the time convergence is investigated by simulations of an 85 vol-% glycerol droplet impacting a solid surface at We = 51. Adaptive time stepping with three different fixed fluid Courant numbers, yielding an increasingly smaller time step length, are tested, namely CFL = 0.25, CFL = 0.125 and CFL = 0.0625. A Δx_{min} of 0.05 mm, using three local adaptive grid refinement levels, is used for all the CFL numbers. The results for the spread factor evolution are presented in Fig. 4, and the implemented framework is time step convergent.

To further investigate the time step dependence of the framework a comparison of both the dynamic contact angle and the contact line velocity is presented in Fig. 5. A CFL of 0.25 does not yield a time step length small enough for the dynamic contact angle to converge. But the results for the two smallest CFL numbers are very similar and the implemented framework is time step convergent for the contact line velocity and the dynamic contact angle.

5.2. Validation of dynamic contact angle models

Two similar test cases, Šikalo et al. (2005a) and German and Bertola (2009), are used to test the framework, and at the same time evaluate and compare the performance of the dynamic contact angle models used. In the experimental study of Šikalo et al. (2005a), an 85 vol-% glycerol droplet is impacting two surfaces of different wettabilities, glass and wax. The glycerol droplet has small static contact angles on the hydrophilic glass surface, $\theta_A = 17°$ and $\theta_R = 13°$, while the angles are more neutral on the wax surface, $\theta_A = 97°$ and $\theta_R = 90°$. The evolution of the spread factor is measured for each model and then compared with experimental data for both   surfaces.   An   impact   Weber   num-

(a) Average dynamic contact angle. The solid black line is the advancing contact angle and the dashed black line is the receding contact angle.

(b) Average contact line velocity.

Fig. 3. Results of average dynamic contact angle and average contact line velocity for the grid convergence study. Four different levels of minimum grid size are investigated.
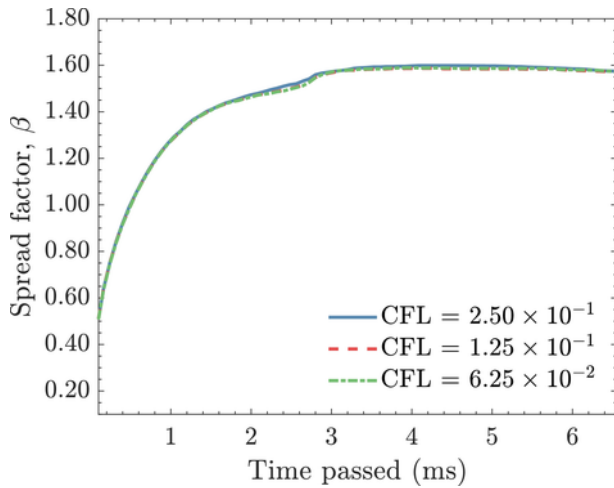
Fig. 4. Results of the spread factor evolution for the time step convergence study. Three time step lengths are investigated.

ber of 51 is used for both surfaces. Relevant physical data of the glycerol droplet used in the validation against Šikalo et al. (2005a) can be found in Table 1. Using the results from the convergence studies, three local adaptive grid refinement levels with a Δx_{min} of 0.05 mm and a fixed fluid Courant number of 0.125 are used in all the simulations in this subsection.

On a slightly hydrophobic wax surface, seen in Fig. 6a, all four models handle the impact quite well. However, while the three truly dynamic models have a good agreement with the experimental data, the quasi-dynamic model cannot accurately capture the dynamics of the spreading and β_{max} ends up being too large. Shikhmurzaev's model predicts the spreading slightly better than does Kistler's model and Cox's model, and the reason is seen in Fig. 6b where the former model yields a larger dynamic contact angle during the spreading phase. The receding phase appears to be best captured by Cox's receding model, which yields a considerably lower dynamic contact angle during the receding phase than the receding model utilised by the two other truly dynamic models. This causes the moving contact line to be almost static during the receding phase, which is a correct prediction as shown by the experimental data. The other two dynamic models also capture the reced-
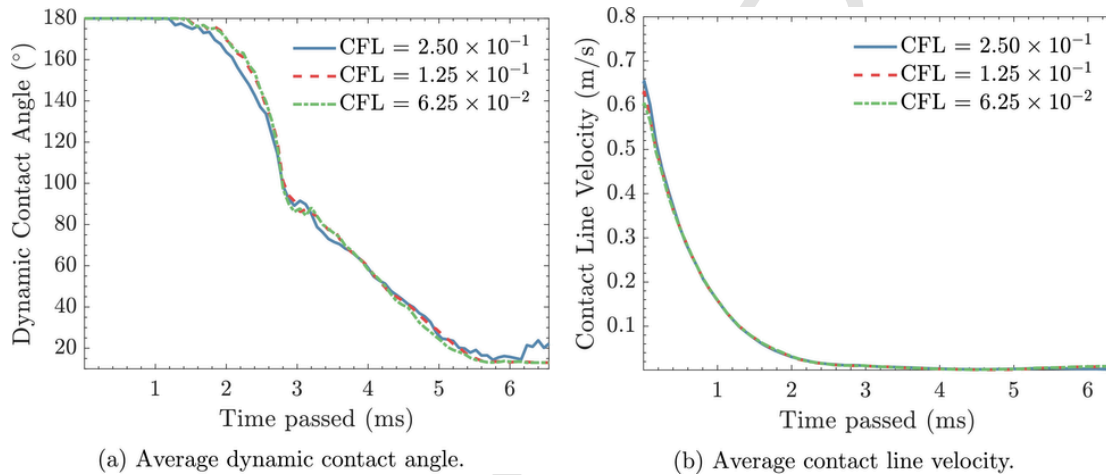

(a) Average dynamic contact angle.

(b) Average contact line velocity.

Fig. 5. Results of average dynamic contact angle and average contact line velocity for the time convergence study. Three different fixed CFL numbers are investigated.
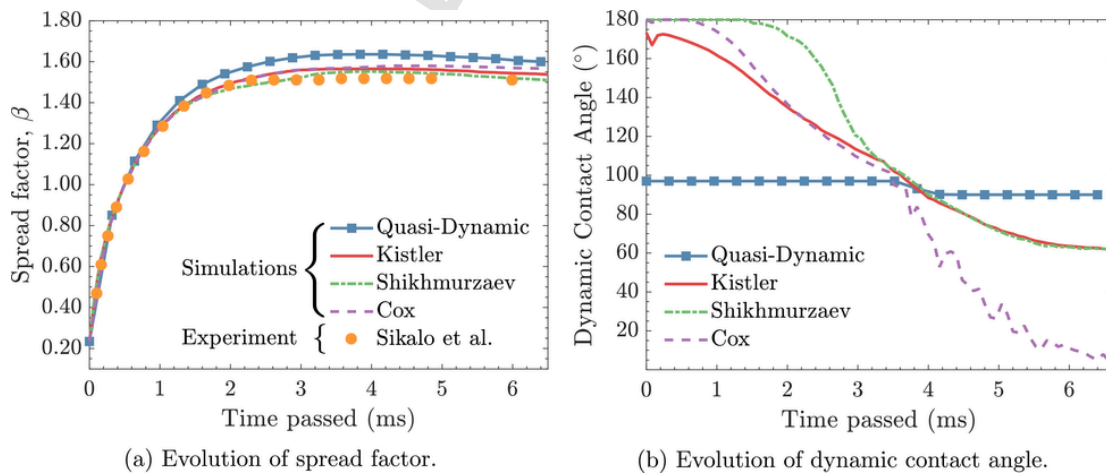

(a) Evolution of spread factor.

(b) Evolution of dynamic contact angle.

Fig. 6. Four different dynamic advancing contact angle models are compared as a glycerol droplet impacts a slightly hydrophobic surface with $\theta_A = 97°$. The left figure compares the spread factor of the four different models to the experimental data of spread factor from Šikalo et al. (2005a). The right figure compares the evolution of the dynamic contact angle for the four models.

ing phase well, while the static receding model of the quasi-dynamic model is slightly worse.

On a hydrophilic surface, $\theta_A = 17°$, there is a considerable difference between the dynamic and quasi-dynamic models, shown in Fig. 7a. The three truly dynamic advancing models follow the experimental data well, while the quasi-dynamic model spreads too much. It clearly shows how a truly dynamic model moderates the spreading phase of the droplet, whereas the constant low advancing contact angle of the quasi-dynamic model yields too much wetting. When comparing the dynamic contact angles from the different models, presented in Fig. 7b, the differences are substantial. The larger initial dynamic contact angle by Shikhmurzaev's model slows down the spreading and yields a better fit to the experimental data than does Kistler's model and Cox's model. The initial larger dynamic contact angle also yields a shorter spreading phase, and shortly after 5 ms the receding phase is reached. The two other dynamic models has a longer spreading phase and reaches the receding phase just before the simulation is terminated at 6.6 ms.

In the experimental study by German and Bertola (2009), three different mixtures of glycerol and water are investigated as they impact on a solid surface, ranging from 80wt-% to 96wt-% glycerol. This yields three Newtonian liquids with varying viscosity, density and surface tension as summarised in Table 3 (German and Bertola, 2009). The maximal spread factor, β_{max}, is measured as the droplets impact at different Weber numbers. In German and Bertola (2009), the droplets are impacting a slightly hydrophobic surface with parafilm-M coating. No advancing or receding contact angles are reported, but a reported equilibrium contact angle of 95° is used as an input for the dynamic contact angle models instead of advancing/receding contact angles. The droplet diameter is 3.1 mm for all mixtures.

The comparison between our simulations and the experimental data from German and Bertola (2009) is presented for the different mixtures of glycerol and water in Figs. 8 and 9. For each We number the performance of the dynamic contact angle models is displayed and compared to the experimental value. In Fig. 8, for the mixture with the lowest viscosity a large overestimation of β_{max} is observed for the quasi-dynamic model, while the dynamic models produce results close to the experimental value of β_{max}. The difference in performance between the quasi-dynamic model and the dynamic models is larger for smaller We numbers, which is to be expected since a smaller We number yields a more surface tension-governed flow. Comparing the dynamic models, Shikhmurzaev's model yields the best description, but the differences are small.

The viscosity will increase with increasing the mass fraction of glycerol, explaining why β_{max} is decreasing in the following figures. In addition, the value of β_{max} does not change much between We = 2 and We = 45 for the different mixtures, as seen in Fig. 9a and b. The three truly dynamic models estimate the maximum spread factor well for both mixtures with high percentage of glycerol, while the quasi-dynamic model overestimates the spreading. As with GL080, the difference in performance between the quasi-dynamic model and the dynamic models is larger for smaller We. The differences between the dynamic models tends to be smaller with increasing viscosity, but a trend can be seen where Shikhmurzaev's model predicts the spreading better. However, the differences between the truly dynamic models are once again small and all three perform very well.

5.3. Comparison of different approaches for treating the receding contact line

Three different approaches of treating the receding contact line are compared to evaluate the importance of a receding contact angle model. The first one is an approach of using a separate dynamic model for the receding contact line, which is termed Dynamic Receding. This is compared to the approach of using a static model, termed Static Receding, and the conventional approach of treating advancing and receding contact lines the same way, termed Conventional. The case compared is the same as in Fig. 6, and Shikhmurzaev's dynamic advancing contact angle model is used as the dynamic advancing contact angle model.

As seen in Fig. 10a, using our approach of a separate dynamic receding model prevents the contact line from receding when the spreading phase is over. And even though experimental data are not available after 6 ms, it is stated in Šikalo et al. (2005b) that the contact line never starts to recede after impact at We = 51. By looking at the common approach instead, it is clearly seen in Fig. 10b how the approach fails to capture contact angle hysteresis. Instead of lowering the dynamic contact angle to prevent the contact line from moving, the dynamic contact angle starts to increase, causing the contact line to recede, when the droplet recoils. The static model performs better than the conventional approach, but the static receding contact angle cannot prevent the contact line from receding. To demonstrate the different behaviours fur-
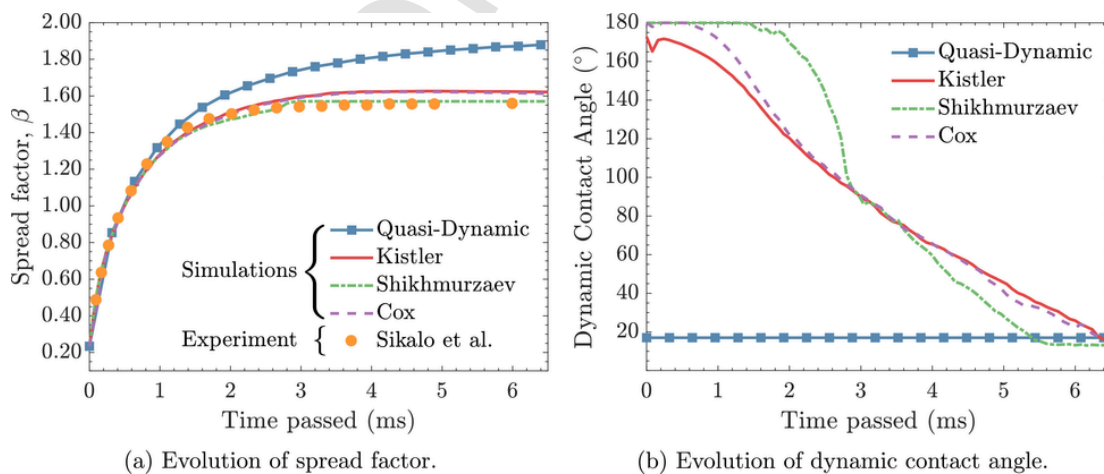

(a) Evolution of spread factor.　　　　　(b) Evolution of dynamic contact angle.

Fig. 7. Four different dynamic contact angle models are compared as a glycerol droplet impacts a hydrophilic surface with $\theta_A = 17°$. The left figure compares the spread factor of the four different dynamic contact angle models to the experimental data of spread factor from Šikalo et al. (2005a). The right figure compares the evolution of the dynamic contact angle for the four models.

Table 3
Physical properties of glycerol/water-mixtures used in simulations.

Abb.	Glycerol	ρ	μ	σ
		(kg/m^3)	(Pa s)	(N/m)
GL080	80wt-%	1210.9	0.056	0.070
GL094	94wt-%	1248.2	0.428	0.074
GL096	96wt-%	1250.8	0.631	0.075
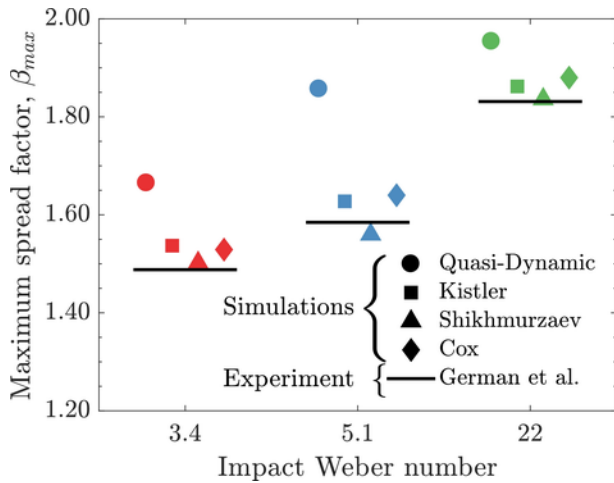
Fig. 8. GL080-droplets impact at three discrete impact Weber numbers. The results of β_{max} from the simulations for all four dynamic contact angle models are compared to experimental values from German and Bertola (2009).

ther, a sequence of the same droplet impact is shown in Fig. 11. The grey droplet half is our Dynamic Receding approach and the black droplet half is the Conventional approach.

As expected, there is no difference between the cases through the spreading phase, up to around 5 ms after impact. But after this point, when the droplet starts to recoil, there is a large difference in behaviour. In Figs. 11d–f, it is seen how the dynamic contact angle of the black droplet starts to increase once again, while it is decreasing for the

grey droplet, as it should be. This shows how an adequate choice of a dynamic contact angle model for the receding contact line is required to be able to capture the contact angle hysteresis phenomena.

5.4. Complex surfaces with mixed wettabilities

A showcase is setup to demonstrate the ability of the framework to handle wetting of complex surfaces, consisting of four hydrophilic plateaus and an underlying hydrophobic surface, as seen in Fig. 12. The plateaus are elevated by 50 μ m and the channels created in between them are 250μm wide. All four plateaus are of square shape and with a side length of 1 mm. The plateaus have contact angles $\theta_A = 10°$ and $\theta_R = 5°$. The underlying surface has contact angles $\theta_A = 165°$ and $\theta_R = 160°$. A droplet is impacting with a velocity of 3 m/s. In the first case the droplet is impacting in the center in between the four plateaus, and in the second case it is impacting the corner of plateau number 1. The droplet has a diameter of 0.33 mm and otherwise the same properties, except for wettability, as stated in Table 1. A fixed fluid Courant number of 0.125 together with a Δx_{min} of 18.75 μ m are used in the simulation. In addition, the importance of a dynamic contact angle model in more complex cases like these are investigated by comparing dynamic models to the quasi-dynamic model.

The impact of the droplet in the center between the plateaus is displayed in a series of frames in Fig. 13, comparing the quasi-dynamic model to Shikhmurzaev's model. The initial spreading is quite similar between the two models, due to the relatively high impact Weber number. The differences between the static and the dynamic model are starting to show at frames (b)–(c), where the dynamic model does not spread as much on the hydrophilic plateaus. This is due to the relatively high dynamic contact angle during the spreading, and the dynamic model therefore spreads more on the hydrophobic surface than the static model. But the hydrophobic surface still acts to minimise the contact area with the liquid, as seen in frame (e), and both the static model and the dynamic model will start to recoil. During the receding phase, frames (d)–(g), the droplet is dewetting the hydrophobic surface while continuing to spread on the hydrophilic plateaus. The constant low contact angle of the static model yields a faster spread on the hydrophilic plateaus, whereas the dynamic model yields a larger mass in the middle. The dewetting of the underlying surface, coupled with the wetting
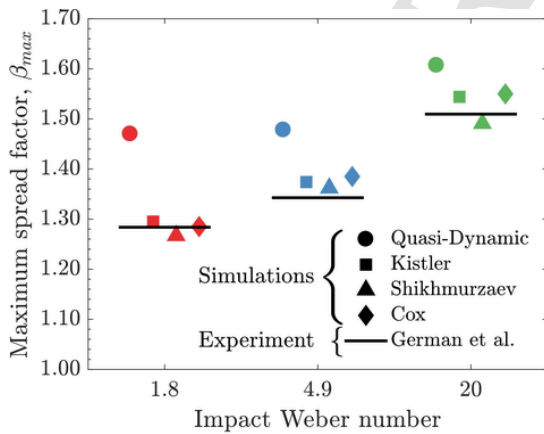
(a) GL094-droplets impact at three discrete impact Weber numbers. The results of β_{max} from the simulations are compared to experimental values from German and Bertola (2009).
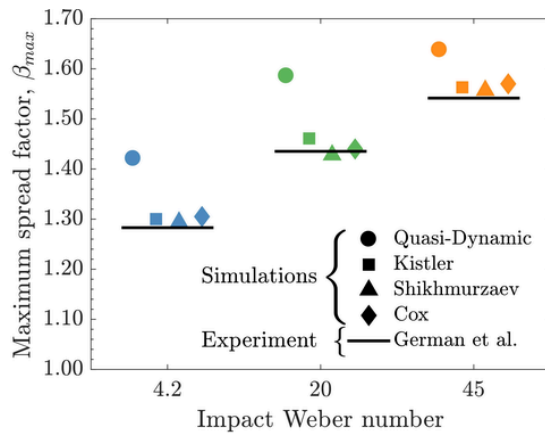
(b) GL096-droplets impact at three discrete impact Weber numbers. The results of β_{max} from the simulations are compared to experimental values from German and Bertola (2009).

Fig. 9. The maximum spread factor comparison for the two most viscous mixtures of glycerol and water. The results from the simulations using each of the four dynamic contact angle models are compared to experimental data from German and Bertola (2009).
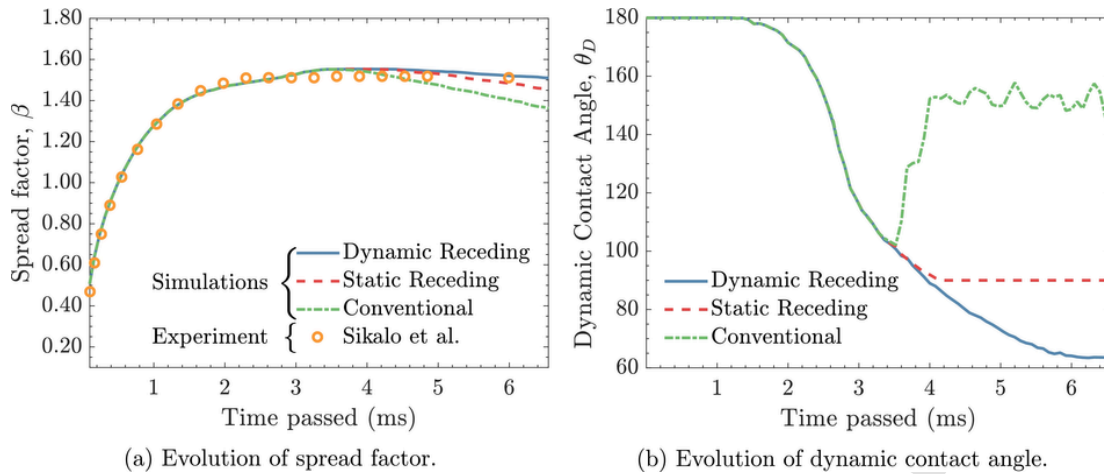
Fig. 10. Comparison of the evolution of spread factor (left) and dynamic contact angle (right) for three different approaches to treat the receding contact line. Our dynamic receding contact angle model (solid line), a static receding contact angle model (dashed line) and the conventional approach of using the same model as for the advancing contact line (dashed dotted line).
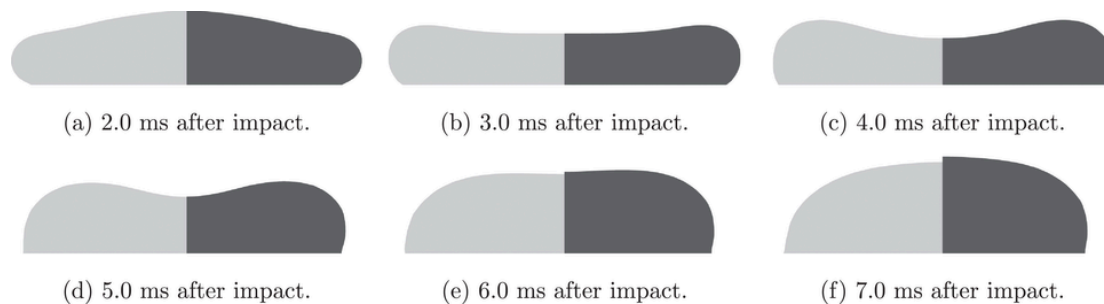

Fig. 11. Sequence of droplet impact. The light grey droplet represents our approach of using a separate dynamic model for the receding contact line. Black is the common approach where the dynamic advancing model is applied on the receding contact line as well. The droplet is spreading through (a) to (d). From (d) to (f) the droplet is recoiling.
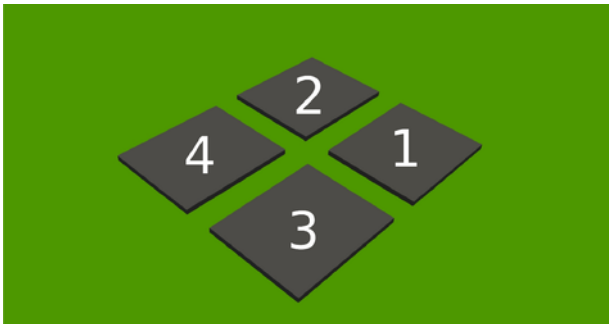

Fig. 12. The part of the printed circuit board used in the showcase simulation. The surface consists of four hydrophilic plateaus and an underlying hydrophobic surface. Two cases with different droplet impacts spots are simulated. The first spot is at the center, in between the four plateaus, and the second spot on the corner, towards the center, of the plateau numbered as 1.

of the plateaus, is eventually causing a breakup of the droplet into four smaller droplets. The time it takes for breakup to occur differs greatly between the two models, since the static model does not account for the contact angle dynamics and therefore enforces a much faster wetting behaviour. The breakup occurs in three steps for both models, decoupling one plateau at the time, which causes a slightly asymmetric final deposition between the four plateaus. The four droplets are then continuing to spread on one plateau each until equilibrium is reached.

The other version of the showcase compares the quasi-dynamic model to Cox's model, and is displayed in a series of frames in Fig. 14. It features a droplet impacting the corner of plateau number 1. After the impact, frames (b)–(d), the use of the quasi-dynamic model makes the droplet spread fast on the targeted plateau. On the other hand, when using the dynamic model the droplet initially faces a large dynamic contact angle on the hydrophilic plateau and therefore spreads more on the hydrophobic surface than when the static model is used. The droplets then spread over to the other plateaus, as shown in frames (d)–(e). The constant low contact angle of the quasi-dynamic model yields a larger spread on the other three plateaus and therefore has a larger droplet mass transferred to them. In frames (f)–(h), the droplets start dewetting the underlying hydrophobic surface and continue to spread on the hydrophilic plateaus, eventually causing breakup to four smaller droplets of varying size. During this phase, the contact line velocities are considerably lower than those during the post impact spreading, and therefore the contact angles from the dynamic model are close to the static contact angle. This causes both models to continue the wetting of the hydrophilic plateaus, as seen in frame (i), but the process is faster for the static model.

To further investigate the differences between the different models on complex surfaces, a comparison was conducted of the droplet spreading on the different plateaus for all the different models. A time evolution is shown of the wetting for the second showcase in Fig. 15. It is seen how the quasi-dynamic model does not capture the wetting dynamics, and spreads a lot more on the neighbouring plateaus than do the dynamic models. A distinct difference between the dynamic models is
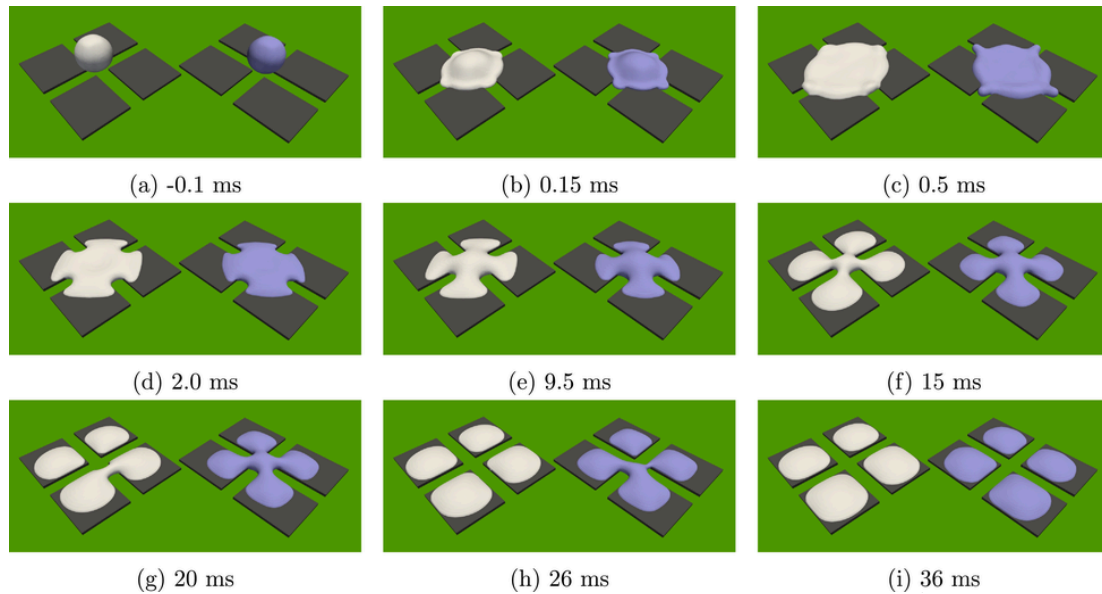
Fig. 13. The grey droplet (left) is using the quasi-dynamic contact angle model, while the purple droplet (right) is using Shikhmurzaev's dynamic contact angle model. The sequence of frames from (a) to (i) show the droplets impacting a surface of varying height and wettability, with time stamps referring to the time after impact. Frames (b)–(d) show initial wetting, (e)–(g) show dewetting of the underlying hydrophobic surface, and (h) to (i) show the breakup and further wetting of the hydrophilic plateaus. (For interpretation of the references to color in this figure legend, the reader is referred to the web version of this article.)
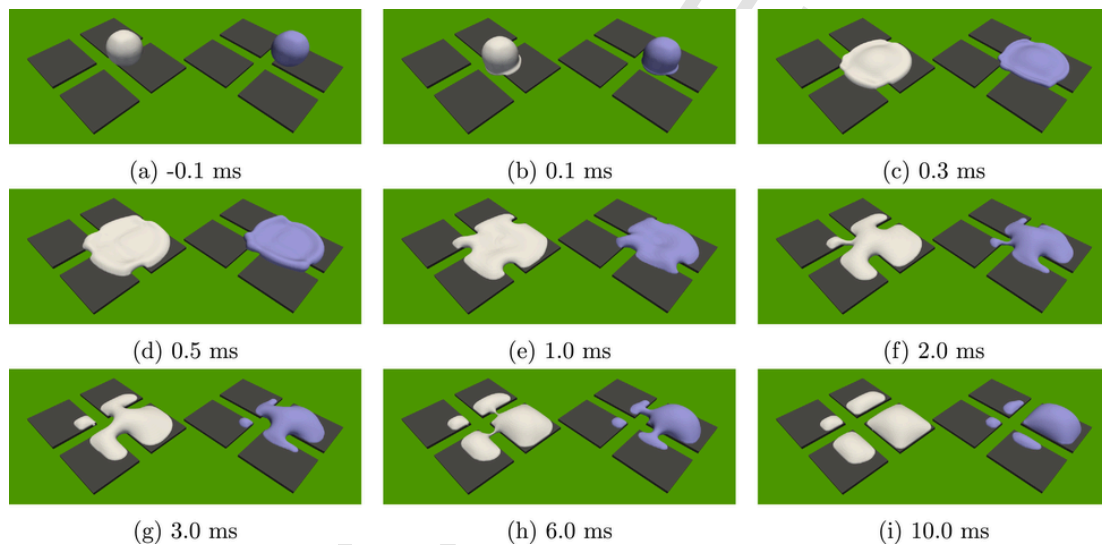

Fig. 14. The grey droplet (left) is using the quasi-dynamic contact angle model, while the purple droplet (right) is using Cox's dynamic contact angle model. The sequence of frames from (a) to (i) show the droplets impacting a surface of varying height and wettability, with time stamps referring to the time after impact. Frames (b)–(d) show initial wetting, (e)–(f) show dewetting of the underlying hydrophobic surface, and (g)–(i) show the breakup and further wetting of the hydrophilic plateaus. (For interpretation of the references to color in this figure legend, the reader is referred to the web version of this article.)

also seen, where Shikhmurzaev's model moderates the spreading to a higher degree, and spreads less on the neighbouring plateaus and considerably slower on the main plateau.

Another important factor is the final distribution of droplet mass across the four plateaus, which is shown in Table 4. While all the models yield close to a 100% wetted area on the first plateau, there is a large variation in the final droplet mass on the plateau. The quasi-dynamic model deposits 73% of the droplet mass on the first plateau, while all the dynamic models leave over 90% of the droplet mass. Comparing the dynamic models, a difference is mainly seen in the spreading on the second and third plateaus. Shikhmurzaev's model

leaves less than half of the droplet mass on these two plateaus compared to Kistler's and Cox's models, which is due to the larger dynamic contact angles of Shikhmurzaev's model. The differences between Cox's model and Kistler's model are very small.

The two versions of the showcase show how the implemented framework can handle dynamic wetting of non-flat surfaces of mixed wettabilities. It also shows the importance of always using a dynamic contact angle model to achieve a better prediction of the wetting dynamics. This is especially true for the initial wetting phase after the impact, where the results differ substantially, but also for the prediction of final droplet deposition, where the results.
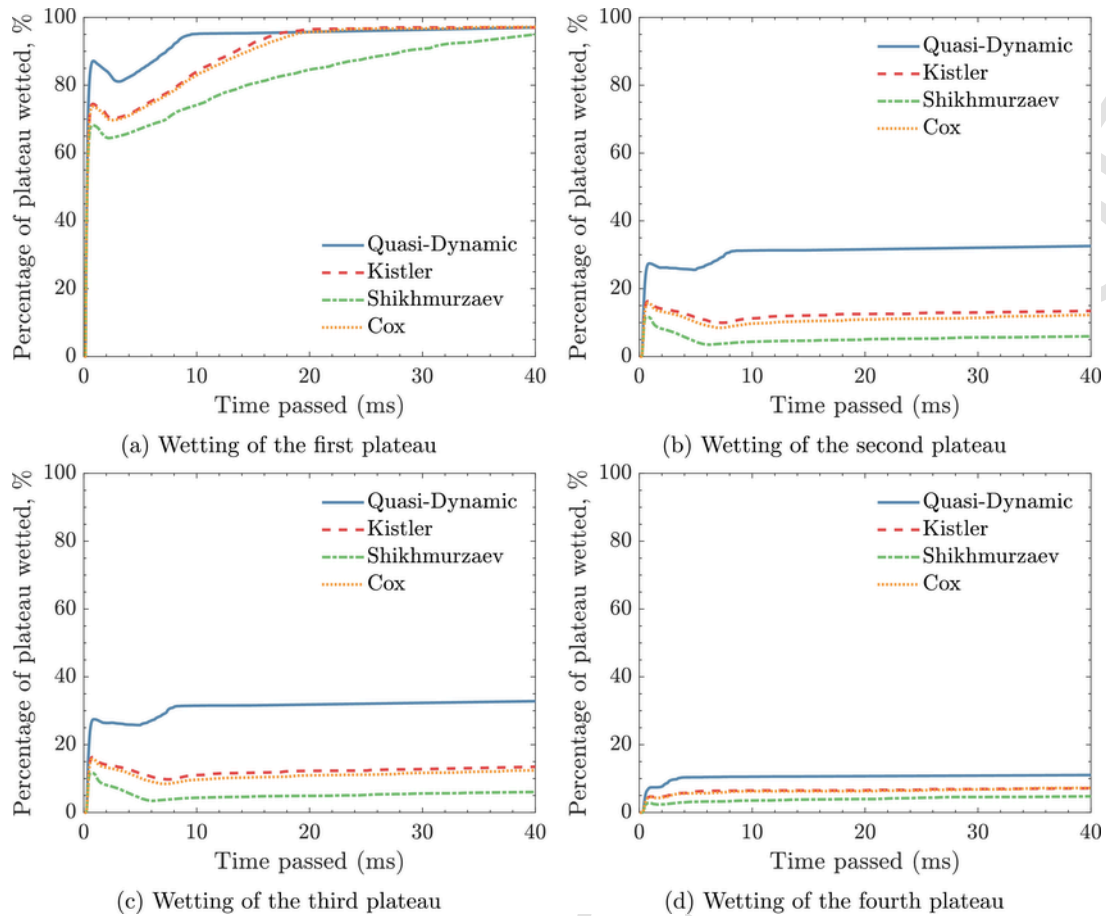
(a) Wetting of the first plateau

(b) Wetting of the second plateau

(c) Wetting of the third plateau

(d) Wetting of the fourth plateau

Fig. 15. Comparison of how the four different models spread on the four plateaus. The droplet impacts on the corner towards the center of the first plateau.

Table 4
Final distribution of droplet mass across the four plateaus for the four different models.

Plateau	Quasi-dynamic	Kistler	Shikhmurzaev	Cox
1	73.2 wt-%	91.2 wt-%	95.8 wt-%	92.1 wt-%
2	11.5 wt-%	3.6 wt-%	1.5 wt-%	3.1 wt-%
3	11.5 wt-%	3.6 wt-%	1.5 wt-%	3.1 wt-%
4	3.8 wt-%	1.6 wt-%	1.2 wt-%	1.7 wt-%

6. Conclusions

We have formulated in this paper an immersed boundary-based framework for dynamic contact angles that is implemented into IBOFLOW as a boundary condition of the Continuum Surface Force method. The framework handles arbitrary surfaces and multiple surfaces of mixed wettabilities for 3D simulations. In order to accurately capture the contact angle hysteresis, different dynamic contact angle models are used on the advancing and the receding contact lines. Four different dynamic contact angle models are tested for advancing contact lines, whereas two different models are tested for receding contact lines. A Navier-slip boundary condition is used at the wetted surface to relax the no-slip boundary and avoid the stress divergence at the contact line. The entire framework, or parts of it, can easily be implemented in other codes with the help of the detailed implementation description.

The convergence in relation to grid size and time step of the implemented framework is investigated by simulations of glycerol droplets impacting a solid surface. The framework is time step convergent, where a relatively low time step (CFL ≤ 0.125) is important for the contact line velocity to converge. The Navier-slip boundary condition enables simulations on finer grids, which is essential for accurate simulations, and yields converging results for droplet spreading. However, the framework still shows a grid dependence for the average dynamic contact angle and the contact line velocity, mainly during the initial spreading of the droplet.

The framework for dynamic contact angle models is validated against experimental data of glycerol droplets with alternating viscosity impacting solid surfaces at low Weber numbers. The overall agreement between the simulations and the experiments is good. For advancing contact lines, we have demonstrated the importance of using a truly dynamic contact angle model to capture the dynamics of the spreading. Of the three truly dynamic contact angle models tested, Shikhmurvaev's model predicts the spreading dynamics best, and especially on hydrophilic surfaces where moderation of the dynamic contact angle is of greater importance. A comparison between our approach of using a separate dynamic contact angle model for receding contact lines to the conventional approach not treating receding contact lines separately is also made. It demonstrates how our framework adequately describes the contact angle hysteresis phenomena and proves the need for a separate dynamic receding contact angle to accurately predict the motion of the receding contact line.

Finally, two showcases are presented in which very complex wetting processes are simulated. They demonstrate the ability of the implemented framework to handle arbitrary surfaces, which is vital for many

industrial applications. It is also shown that the framework can handle adjacent surfaces of very different wettability, which is especially important for the newly emerging field of superhydrophobic coatings. The cases also demonstrate the need of dynamic contact angle models for complex wetting cases as well, since a static model is not capable of capturing the dynamics of wetting and dewetting.

Acknowledgement

References

Afkhami, S., Zaleski, S., Bussmann, M., 2009. A mesh-dependent model for applying dynamic contact angles to vof simulations. J. Comput. Phys. 228 (15), 5370–5389. https://doi.org/10.1016/j.jcp.2009.04.027.

Andrade, R., Skurtys, O., Osorio, F., 2013. Drop impact behavior on food using spray coating: fundamentals and applications. Food Res. Int. 54 (1), 397–405 https://doi.org/10.1016/j.foodres.2013.07.042.

Ashish Saha, A., Mitra, S.K., 2009. Effect of dynamic contact angle in a volume of fluid (vof) model for a microfluidic capillary flow. J. Colloid Interface Sci. 339 (2), 461–480. https://doi.org/10.1016/j.jcis.2009.07.071.

B. Dussan V., B.E., 1976. The moving contact line: the slip boundary condition. J. Fluid Mech. 77, 665–684.

Blake, T., Shikhmurzaev, Y., 2002. Dynamic wetting by liquids of different viscosity. J. Colloid Interface Sci. 253 (1), 196–202. https://doi.org/10.1006/jcis.2002.8513.

Bostanci, H., Rini, D.P., Kizito, J.P., Chow, L.C., 2009. Spray cooling with ammonia on microstructured surfaces: performance enhancement and hysteresis effect. J. Heat Transfer 131 (7), 071401. https://doi.org/10.1115/1.3089553.

Brackbill, J., Kothe, D., Zemach, C., 1992. A continuum method for modeling surface tension. J. Comput. Phys. 100 (2), 335–354. https://doi.org/10.1016/0021-9991(92)90240-y.

Bussmann, M., Chandra, S., Mostaghimi, J., 2000. Modeling the splash of a droplet impacting a solid surface. Phys. Fluids 12 (12), 3121. https://doi.org/10.1063/1.1321258.

Chandra, S., di Marzo, M., Qiao, Y., Tartarini, P., 1996. Effect of liquid-solid contact angle on droplet evaporation. Fire Saf. J. 27 (2), 141–158 https://doi.org/10.1016/S0379-7112(96)00040-9.

Cox, R.G., 1986. The dynamics of the spreading of liquids on a solid surface. Part 1. Viscous flow. J. Fluid Mech. 168, 169194. https://doi.org/10.1017/S0022112086000332.

Cox, R.G., 1998. Inertial and viscous effects on dynamic contact angles. J. Fluid Mech. 357, 249278. https://doi.org/10.1017/S0022112097008112.

Dupont, J.-B., Legendre, D., 2010. Numerical simulation of static and sliding drop with contact angle hysteresis. J. Comput. Phys. 229 (7), 2453–2478. doi: https://doi.org/10.1016/j.jcp.2009.07.034

Dussan V., V.E.B., Ramé, E., Garoff, S., 1991. On identifying the appropriate boundary conditions at a moving contact line: an experimental investigation. J. Fluid Mech. 230, 97116. https://doi.org/10.1017/S0022112091000721.

Ferrás, L., Nóbrega, J., Pinho, F., 2013. Implementation of slip boundary conditions in the finite volume method: new techniques. Int. J. Numer. Methods Fluids 72 (7), 724–747. https://doi.org/10.1002/fld.3765.

German, G., Bertola, V., 2009. Review of drop impact models and validation with high-viscosity newtonian fluids. Atomization Sprays 19 (8), 787–807.

Göhl, J., Markstedt, K., Mark, A., Håkansson, K., Gatenholm, P., Edelvik, F., 2018. Simulations of 3d bioprinting: predicting bioprintability of nanofibrillar inks. Biofabrication 10 (3), 034105. doi: https://doi.org/10.1088/1758-5090/aac872

Hirt, C., Nichols, B., 1981. Volume of fluid (vof) method for the dynamics of free boundaries. J. Comput. Phys. 39 (1), 201–225. https://doi.org/10.1016/0021-9991(81)90145-5.

Hocking, L.M., Rivers, A.D., 1982. The spreading of a drop by capillary action. J. Fluid Mech. 121, 425442. https://doi.org/10.1017/S0022112082001979.

Hoffman, R.L., 1975. A study of the advancing interface. I. Interface shape in liquid-gas systems. J. Colloid Interface Sci. 50 (2), 228–241. https://doi.org/10.1016/0021-9797(75)90225-8.

Holmgren, H., 2015. Towards accurate modeling of moving contact lines. Uppsala University, Licentiate Thesis.

Johnson, R.E., Dettre, R.H., Brandreth, D.A., 1977. Dynamic contact angles and contact angle hysteresis. J. Colloid Interface Sci. 62 (2), 205–212. doi: https://doi.org/10.1016/0021-9797(77)90114-X

Johnson, T., Röyttä, P., Mark, A., Edelvik, F., 2016. Simulation of the spherical orientation probability distribution of paper fibers in an entire suspension using immersed boundary methods. J. Nonnewton. Fluid Mech. 229, 1–7. https://doi.org/10.1016/j.jnnfm.2016.01.001.

Kistler, S.F., 1993. Hydrodynamics of wetting. In: Berg, J.C. (Ed.), Wettability. 49, M. Dekker, New York, p. 311.

Lalia, B.S., Janajreh, I., Hashaikeh, R., 2017. A facile approach to fabricate superhydrophobic membranes with low contact angle hysteresis. J. Memb. Sci. 539, 144–151 https://doi.org/10.1016/j.memsci.2017.05.071.

Legendre, D., Maglio, M., 2015. Comparison between numerical models for the simulation of moving contact lines. Comput. Fluids 113, 2–13. https://doi.org/10.1016/j.compfluid.2014.09.018.

Liu, H.-R., Ding, H., 2015. A diffuse-interface immersed-boundary method for two-dimensional simulation of flows with moving contact lines on curved substrates. J. Comput. Phys. 294, 484–502. doi: https://doi.org/10.1016/j.jcp.2015.03.059

Maglio, M., Legendre, D., 2014. Numerical simulation of sliding drops on an inclined solid surface. In: Sigalotti, G.L.D., Klapp, J., Sira, E. (Eds.), Computational and Experimental Fluid Mechanics with Applications to Physics, Engineering and the Environment. Springer International Publishing, pp. 47–69. https://doi.org/10.1007/978-3-319-00191-3_3.

Malgarinos, I., Nikolopoulos, N., Marengo, M., Antonini, C., Gavaises, M., 2014. Vof simulations of the contact angle dynamics during the drop spreading: standard models and a new wetting force model. Adv. Colloid Interface Sci. 212, 1–20. https://doi.org/10.1016/j.cis.2014.07.004.

Mangini, D., Antonini, C., Marengo, M., Amirfazli, A., 2015. Runback ice formation mechanism on hydrophilic and superhydrophobic surfaces. Cold. Reg. Sci. Technol. 109, 53–60 https://doi.org/10.1016/j.coldregions.2014.09.012.

Mark, A., Andersson, B., Tafuri, S., Engström, K., Söröd, H., Edelvik, F., Carlson, J.S., 2013. Simulation of electrostatic rotary bell spray painting in automotive paint shops. Atomization Sprays 23 (1), 25–45. https://doi.org/10.1615/atomizspr.2013006232.

Mark, A., Bohlin, R., Segerdahl, D., Edelvik, F., Carlson, J.S., 2014. Optimisation of robotised sealing stations in paint shops by process simulation and automatic path planning. Int. J. Manuf. Res. 9 (1), 4–26. https://doi.org/10.1504/ijmr.2014.059597.

Mark, A., Rundqvist, R., Edelvik, F., 2011. Comparison between different immersed boundary conditions for simulation of complex fluid flows. Fluid Dyn. Mater. Process. 7, 241–258.

Mark, A., van Wachem, B.G., 2008. Derivation and validation of a novel implicit second-order accurate immersed boundary method. J. Comput. Phys. 227 (13), 6660–6680. https://doi.org/10.1016/j.jcp.2008.03.031.

Mathieu, B., 2003. Etudes physique, expérimentale et numérique des mécanismes de base intervenant dans leséctoulements diphasiques en micro-fluidique. Université de Provence-Marseille, Thèse de doctorat.

Ngan, C.G., Dussan V., E.B., 1982. On the nature of the dynamic contact angle: an experimental study. J. Fluid Mech. 118, 2740. https://doi.org/10.1017/S0022112082000949.

Nichita, B.A., Zun, I., Thome, J.R., 2010. A vof method coupled with a dynamic contact angle model for simulation of two-phase flows with partial wetting. 7th International Conference on Multiphase Flow, ICMF 2010.

Pasandideh-Fard, M., Pershin, V., Chandra, S., Mostaghimi, J., 2002. Splat shapes in a thermal spray coating process: simulations and experiments. J. Therm. Spray Technol. 11 (2), 206–217. https://doi.org/10.1361/105996302770348862.

Popescu, M.N., Ralston, J., Sedev, R., 2008. Capillary rise with velocity-dependent dynamic contact angle. Langmuir 24 (21), 12710–12716. https://doi.org/10.1021/la801753t.

Renardy, M., Renardy, Y., Li, J., 2001. Numerical simulation of moving contact line problems using a volume-of-fluid method. J. Comput. Phys. 171 (1), 243–263. https://doi.org/10.1006/jcph.2001.6785.

Rhie, C.M., Chow, W.L., 1983. Numerical study of the turbulent flow past an airfoil with trailing edge separation. AIAA J. 21 (11), 1525–1532. https://doi.org/10.2514/3.8284.

Roisman, I., Opfer, L., Tropea, C., Raessi, M., Mostaghimi, J., Chandra, S., 2008. Drop impact onto a dry surface: role of the dynamic contact angle. Colloids Surf., A 322 (1–3), 183–191. https://doi.org/10.1016/j.colsurfa.2008.03.005.

Rosengarten, G., Harvie, D., Cooper-White, J., 2006. Contact angle effects on micro-droplet deformation using cfd. Appl. Math. Model. 30 (10), 1033–1042. https://doi.org/10.1016/j.apm.2005.06.011.

Sharifahmadian, O., Salimijazi, H., Fathi, M., Mostaghimi, J., Pershin, L., 2013. Relationship between surface properties and antibacterial behavior of wire arc spray copper coatings. Surf. Coat. Technol. 233, 74–79. Mechanical and Tribological Properties of Biomedical Coatings and Surface-modified Biomaterials. https://doi.org/10.1016/j.surfcoat.2013.01.060.

Shikhmurzaev, Y.D., 1994. Mathematical modeling of wetting hydrodynamics. Fluid Dyn. Res. 13 (1), 45–64. https://doi.org/10.1016/0169-5983(94)90063-9.

Shikhmurzaev, Y.D., 2008. Capillary Flows With Forming Interfaces. Chapman & Hall/CRC.

Soltman, D., Smith, B., Morris, S., Subramanian, V., 2013. Inkjet printing of precisely defined features using contact-angle hysteresis. J. Colloid Interface Sci. 400, 135–139 https://doi.org/10.1016/j.jcis.2013.03.006.

Sui, Y., Ding, H., Spelt, P.D., 2014. Numerical simulations of flows with moving contact lines. Annu. Rev. Fluid Mech. 46 (1), 97–119. https://doi.org/10.1146/annurev-fluid-010313-141338.

Sui, Y., Spelt, P.D., 2013. An efficient computational model for macroscale simulations of moving contact lines. J. Comput. Phys. 242, 37–52. doi: https://doi.org/10.1016/j.jcp.2013.02.005

Svenning, E., Mark, A., Edelvik, F., Glatt, E., Rief, S., Wiegmann, A., Martinsson, L., Lai, R., Fredlund, M., Nyman, U., 2012. Multiphase simulation of fiber suspension flows using immersed boundary methods. Nordic Pulp Paper Res. J. 27 (02), 184–191. https://doi.org/10.3183/npprj-2012-27-02-p184-191.

Tanner, L.H., 1979. The spreading of silicone oil drops on horizontal surfaces. J. Phys. D Appl. Phys. 12 (9), 1473.

Ubbink, O., 1997. Numerical prediction of two fluid systems with sharp interfaces. University of London, Ph.D. Thesis.

Ubbink, O., Issa, R., 1999. A method for capturing sharp fluid interfaces on arbitrary meshes. J. Comput. Phys. 153 (1), 26–50. https://doi.org/10.1006/jcph.1999.6276.

Van Doormaal, J.P., Raithby, G.D., 1984. Enhancements of the simple method for predicting incompressible fluid flows. Numer. Heat Transfer, Part B 7 (2), 147–163. https://doi.org/10.1080/10407798408546946.

Šikalo, , Tropea, C., Ganic, E., 2005. Dynamic wetting angle of a spreading droplet. Exp. Therm Fluid Sci. 29 (7), 795–802. https://doi.org/10.1016/j.expthermflusci.2005.03.006.

Šikalo, , Wilhelm, H.-D., Roisman, I.V., Jakirlić, S., Tropea, C., 2005. Dynamic contact angle of spreading droplets: experiments and simulations. Phys. Fluids 17 (6), 62–103. https://doi.org/10.1063/1.1928828.

Yan, H., Yuanhao, W., Hongxing, Y., 2017. Teos/silane coupling agent composed double layers structure: a novel super-hydrophilic coating with controllable water contact angle value. Appl. Energy 185, 2209–2216 https://doi.org/10.1016/j.apenergy.2015.09.097.

Young, T., 1805. An essay on the cohesion of fluids. Philos. Trans. R. Soc. Lond. 95 (0), 65–87. https://doi.org/10.1098/rstl.1805.0005.

Zhao, J., Chen, S., Liu, Y., 2017. Dynamical behaviors of droplet impingement and spreading on chemically heterogeneous surfaces. Appl. Surf. Sci. 400, 515–523 https://doi.org/10.1016/j.apsusc.2016.12.209.